Research Article

Counterion Tuning of Near-Infrared Organic Salts Dictates Phototoxicity to Inhibit Tumor Growth

Deanna Broadwater, Hyllana C. D. Medeiros, Matthew Bates, Amir Roshanzadeh, Shao Thing Teoh, Martin P. Ogrodzinski, Babak Borhan, Richard R. Lunt,* and Sophia Y. Lunt*

Cite This: ACS Appl. Mater. Interfaces 2022, 14, 53511−53522

Read Online

ACCESS | Metrics & More | Article Recommendations | Supporting Information

ABSTRACT: Photodynamic therapy (PDT) has the potential to improve cancer treatment by providing dual selectivity through the use of both photoactive agent and light, with the goal of minimal harmful effects from either the agent or light alone. However, current PDT is limited by insufficient photosensitizers (PSs) that can suffer from low tissue penetration, insufficient phototoxicity (toxicity with light irradiation), or undesirable cytotoxicity (toxicity without light irradiation). Recently, we reported a platform for decoupling optical and electronic properties with counterions that modulate frontier molecular orbital levels of a photoactive ion. Here, we demonstrate the utility of this platform *in vivo* by pairing near-infrared (NIR) photoactive heptamethine cyanine cation (Cy^+), which has enhanced optical properties for deep tissue penetration, with counterions that make it cytotoxic, phototoxic, or nontoxic in a mouse model of breast cancer. We find that pairing Cy^+ with weakly coordinating anion $FPhB^-$ results in a selectively phototoxic PS (CyFPhB) that stops tumor growth *in vivo* with minimal side effects. This work provides proof of concept that our counterion pairing platform can be used to generate improved cancer PSs that are selectively phototoxic to tumors and nontoxic to normal healthy tissues.

KEYWORDS: photodynamic therapy, heptamethine cyanine, photosensitizer, metastatic breast cancer, near-infrared
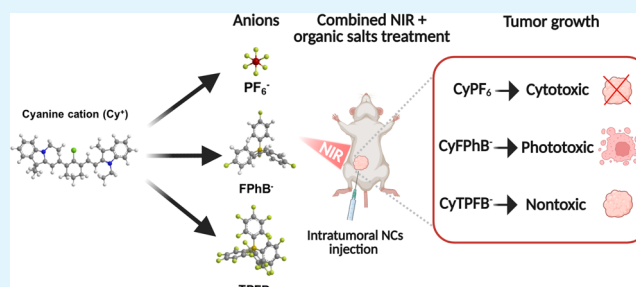
INTRODUCTION

The lack of targeted therapy options remains a major problem for the effective treatment of many cancer types, and nonspecific chemotherapy leads to harsh side effects due to unintended toxicity in normal tissues.[1] A promising solution is photodynamic therapy (PDT), which uses light-activated photosensitizers (PSs) to treat tumors by the generation of reactive oxygen species (ROS) upon photoexcitation.[2−4] PSs that absorb and emit in the near-infrared (NIR) range (650−1200 nm) display superior tissue penetration and reduced photodamage by avoiding visible light wavelengths (400−650 nm) absorbed by biological tissue components.[5−9]

Cyanines are commonly used NIR scaffolds due to their ease of synthesis, structural tunability, and biocompatibility.[10−13] For example, indocyanine green is an NIR heptamethine cyanine used in diagnostic clinical cancer studies for sentinel lymph node mapping to detect metastasis.[14] However, it suffers from poor chemical stability, nonspecific binding, and off-target toxicity, resulting in limited medical usage.[15,16] Indeed, this is a common problem in cancer therapy: even with tumor-targeting approaches such as nanoparticle formulation or antibody conjugation, chemotherapeutics can still accumulate in healthy tissues, notably the liver.[17−19] PDTs with PSs such as Photofrin (porfimer sodium) and Foscan (mTHPC, temoporfin) have displayed offsite cytotoxicity

(toxicity without light irradiation), preventing their use in the treatment of many cancers.[20,21] Therefore, despite advances in tumor targeting, there is a need for NIR-PSs with selective phototoxicity (toxicity with light irradiation) and minimal cytotoxicity in normal tissues.

In addition to their improved NIR optical properties, cyanines have inherent tumor-targeting capabilities, in large part due to their uptake by organic anion transporter polypeptides (OATPs; human, Oatps; rodent).[22,23] OATPs are cellular transporters that mediate the uptake of numerous amphipathic endogenous and exogenous molecules; they are expressed throughout the body in a wide range of tissues and play a critical role in drug uptake and biodistribution.[24] OATPA1/B1 and OATP2B1 transporters, which mediate the uptake of cancer chemotherapeutics, are upregulated in a number of cancer cells and are regulated by hypoxia-inducible factor 1α (HIF-1α), a transcription factor commonly expressed in the hypoxic tumor environment.[25,26] PDT *in vitro* studies
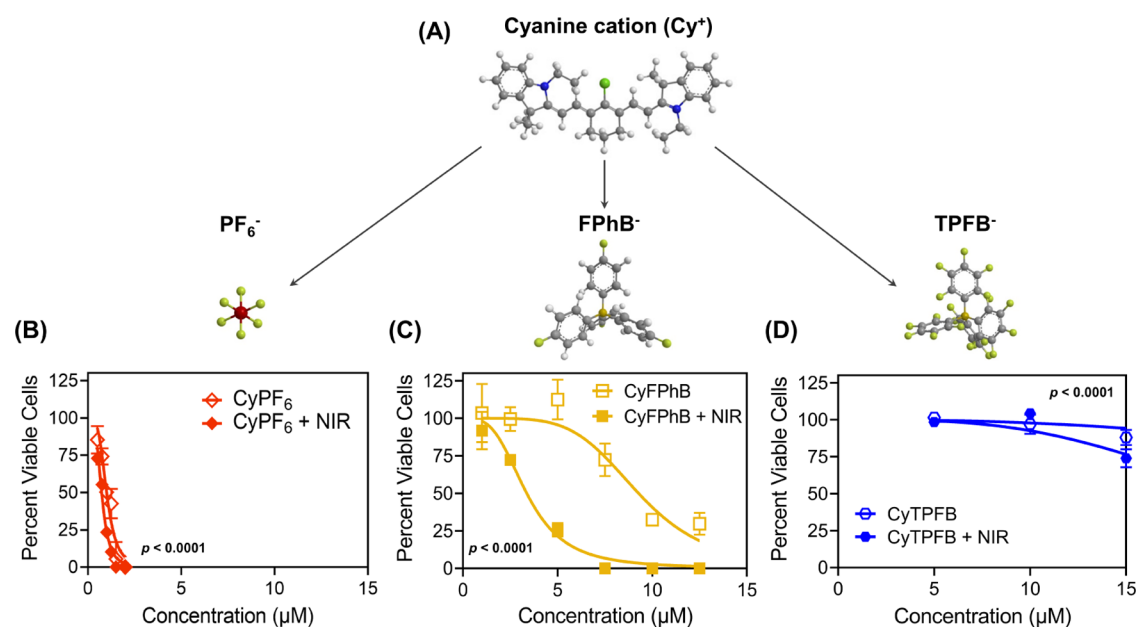
Figure 1. Fluorescent organic salts can be used as photosensitizing agents to treat breast cancer cells. Mouse mammary cancer cells (6DT1) were incubated with the indicated concentrations of organic salt pairings with or without near-infrared (NIR, 850 nm) irradiation to determine half-maximal inhibitory concentrations (IC_{50}). (A) Photoactive heptamethine cyanine cation (Cy^+) is tuned with counterions to modulate toxicity. Percent of viable cells was determined for (B) $CyPF_6$ ($CyPF_6$), (C) CyFPhB ($CyC_{24}H_{16}BF_4$), and (D) CyTPFB ($CyC_{24}BF_{20}$). Data are displayed as means $\pm$ S.E.M., n = 3. Statistical significance (p-values) of IC_{50} shifts (dark IC_{50} vs NIR IC_{50}) are displayed in graphs.

with cyanine dyes frequently assess cancer uptake specificity with inhibition assays of OATPA1/B1 and OATP2B1 transporters.[27,28] In addition to OATPs, recent studies suggest that serum albumin may be an overlooked mediator of cyanine's tumor-targeting capabilities. Albumin is the predominant protein in the blood and is responsible for maintaining osmotic pressure and chaperoning endogenous molecules through the vasculature system.[29] Albumin is reported to have increased tumor accumulation due to upregulated albumin catabolism that fuels cancer growth.[30] Recent studies report that mesochlorinated cyanines can covalently bind to albumin and that cyanine albumin adducts accumulate within the tumor interstitium.[31,32] Albumin is a commonly used targeting moiety for chemotherapeutics and nanomaterials; thus, albumin conjugation may contribute to the tumor-targeting ability of cyanine dyes.[33,34] To assess the mechanisms of tumor targeting, biodistribution, and potential translatability of our findings to additional cancers and preclinical models, we also characterize uptake mediated by mouse Oatps and albumin in vitro.

We recently reported a platform to modulate the toxicity of NIR photoactive heptamethine cyanine cation (Cy^+) by counterion pairing with weakly coordinating anions in nanoparticle formulations.[35] The dipole-modulating counterions modify the frontier molecular orbital energy without changing the band gap. This allows for independent modification of electronic properties from optical properties, resulting in the ability to adjust the toxicity of organic salts without affecting their optical properties such as absorption, emission, and Stokes shift. The composition of photoactive salts is locked in cellular environments by the formation of nanoparticles (average diameter of ~4 nm) that prevent cation−anion dissociation.[35] Indeed, pairing Cy^+ with small, hard anions produces organic salts that are cytotoxic, while pairing with bulky, weakly coordinating halogenated anions produces organic salts that are either phototoxic and

noncytotoxic, or nonphototoxic and noncytotoxic, in human lung carcinoma cells and metastatic human melanoma cell lines.[35] This novel engineering platform through counterion pairing could be used to design PS agents specifically for PDT with low cytotoxicity and high phototoxicity. While we introduced the utility of PS agents in vitro using human cancer cell lines,[35] we have not previously demonstrated their ability to stop tumor growth in vivo using mouse models of cancer.

Here, we tested the hypothesis that our toxicity-tuning platform via counterions can be used to design a PS with low cytotoxicity and high phototoxicity for in vivo PDT. We used a clinically relevant orthotopic mouse model of metastatic breast cancer: 6DT1 cells derived from an MMTV-Myc-driven tumor injected into the fourth mammary fat pad of syngeneic FVB mice.[36] This model allowed for the testing of counterion-tuned PSs in a physiologically relevant tumor microenvironment in immunocompetent mice, as both the tumor microenvironment and a functional immune system are critical for metastasis and PDT pharmacodynamics studies.[37−40] Furthermore, metastatic breast cancer has poor patient prognoses with limited targeted therapies available only for specific subtypes, making it an attractive candidate for PDT.[41] Using an orthotopic mouse model of breast cancer, we tested PDT in vivo using Cy^+ paired with three different representative toxicity-tuning anions: hexafluorophosphate (PF_6^-), tetrakis (4-fluorophenyl) borate ($FPhB^-$: $C_{24}H_{16}BF_4^-$), and tetrakis (pentafluorophenyl) borate ($TPFB^-$: $C_{24}BF_{20}^-$) (Figure 1A). The mean aggregate sizes of $CyPF_6$, CyFPhB, and CyTPFB range from 5 to 9 nm (Figure S1). We found that our previous in vitro results in human lung carcinoma and melanoma cell lines were reproducible both in vitro and in vivo in a metastatic breast cancer model, with comparable trends for cytotoxic ($CyPF_6$), phototoxic (CyFPhB), and less toxic (CyTPFB) anion pairings. We further assessed all three organic salts based on in vivo pharmacokinetics, antitumor efficacy with light irradiation, and offsite toxicity. These organic salts all displayed tumor-specific
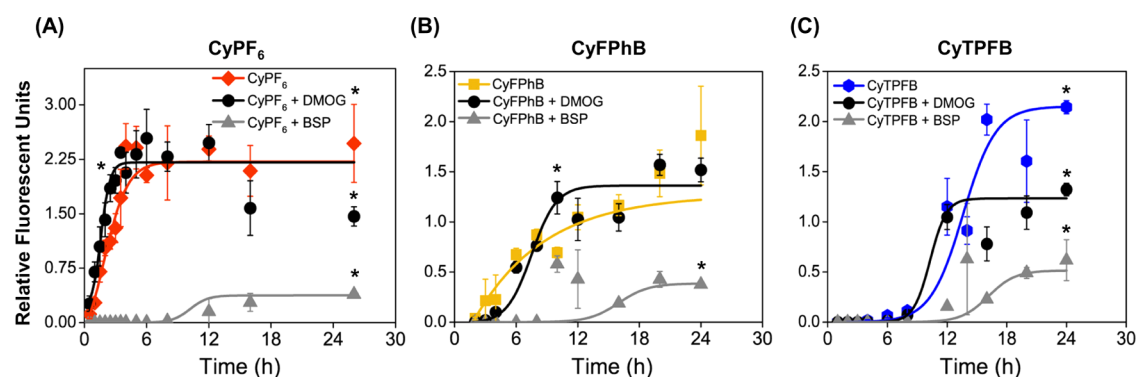
Figure 2. Organic anion transporter polypeptides (Oatps) mediate the cellular uptake of CyPF$_6$ but only partially account for CyTPFB and CyFPhB uptakes. 6DT1 cells were preincubated with 1 mM dimethyloxalylglycine (DMOG), a HIF-1α stabilizer, or 250 μM bromosulfophthalein (BSP), a competitive Oatps inhibitor. Following preincubation with Oatps modulating drugs, cells were incubated with the indicated organic salt for 25 h. Relative fluorescence units were measured for (A) 1 μM CyPF$_6$, (B) 5 μM CyFPhB, and (C) 15 μM CyTPFB. Data are displayed as means $\pm$ S.D., n = 3. Statistically significant differences (p-value <0.05) are marked with asterisks. Curves were fit using a sigmoidal dose−response function using Origin Pro8. Sigmoidal curve fitting values are shown in Table S3.

accumulation *in vivo*, and CyFPhB was the most potent PS agent with enhanced phototoxicity that eliminates tumor growth upon NIR excitation with minimal side effects in mice. These *in vivo* results validate our counterion tuning strategy, which has the potential to expand the clinical applications of cancer PDT agents.

RESULTS AND DISCUSSION

Counterion Tuning of Organic Salts Controls Toxicity during Photodynamic Therapy of Mouse Metastatic Mammary Cancer Cells *In Vitro*. To confirm that our previous *in vitro* findings from A549 human lung cancer and WM1158 melanoma cell lines can be translated to an *in vivo* mouse model of breast cancer, we first performed *in vitro* PDT on 6DT1 mouse mammary carcinoma cells following incubation with various concentrations of CyPF$_6$, CyFPhB, and CyTPFB with or without 850 nm light irradiation.[35] Consistent with our previous results in A549 and WM1158 cells, we found CyPF$_6$ to be cytotoxic, CyFPhB to be phototoxic, and CyTPFB to be minimally toxic in 6DT1 cells. CyPF$_6$ is cytotoxic in 6DT1 cells at low concentrations: cell death occurs independent of NIR irradiation with similar half-maximal inhibitory concentration (IC$_{50}$) values of 1 μM (dark IC$_{50}$) and 0.7 μM (NIR IC$_{50}$) without and with light irradiation, respectively (Figure 1B and Table S1). CyFPhB is highly phototoxic with low cytotoxicity, with a dark IC$_{50}$ of 9 μM and an NIR IC$_{50}$ of 3 μM (Figure 1C and Table S1). At higher concentrations, organic salts are cytotoxic even in the absence of light excitation due to the persistent generation of low levels of mitochondrial ROS (Figure S2). With a dark IC$_{50}$ that is three times the concentration of the NIR IC$_{50}$, CyFPhB is a promising candidate for *in vivo* PDT applications. CyTPFB displayed minimal cytotoxicity and minor phototoxicity with a dark IC$_{50}$ of 45 μM and an NIR IC$_{50}$ of 22 μM (Figure 1D and Table S1). While there is a twofold difference in dark and NIR IC$_{50}$ of CyTPFB, an NIR IC$_{50}$ concentration of 22 μM is too high to achieve *in vivo* and is therefore not ideal for PDT applications.[42]

Oatps and Albumin Mediate Cellular Uptake of Fluorescent Organic Salts. Next, we investigated the roles of Oatps and albumin in mediating the cancer cell uptake of fluorescent organic salts and verified their relevance in our model. As discussed above, human OATPs and albumin have

been shown to mediate the uptake of cyanine dyes. Data from Gene Expression Omnibus (GEO) show that 6DT1 tumors and cells in culture express the gene product of mouse Oatp1b2 (Slco1b2), which has 65% amino acid sequence homology with human OATP1B1 (Table S2).[43] In addition to Oatp1b2 expression, 6DT1 tumors and cells express higher levels of proteins that uptake albumin, including secreted protein acidic and rich in cysteine (Sparc), compared to surrounding breast tissues (Table S2).[44,45] These expression data show that our 6DT1 model reflects expression trends found in human breast cancer and is therefore appropriate and clinically relevant for investigating Oatp- and albumin-mediated cellular uptakes of cyanine organic salts.

To assess the role of Oatps on organic salt uptake in our breast cancer model, 6DT1 cells were preincubated in cell media with 250 μM bromosulfophthalein (BSP), a competitive inhibitor of Oatps, or 1 mM dimethyloxalylglycine (DMOG), a HIF-1α stabilizer to increase the expression of Oatps.[25,31,46,47] Following drug preincubation, organic salts were added to cell media, and intracellular fluorescence was measured at various time points to determine cellular uptake. Fluorescence over time was plotted and fitted with a sigmoidal curve to determine uptake kinetics. Nanoparticle absorption spectra were monitored using ultraviolet−visible (UV−Vis) spectroscopy to confirm that the addition of chemical agents did not affect nanoparticle composition or stability (Figure S3). Cellular uptake of CyPF$_6$ increased rapidly upon addition to media, reached a maximal uptake at 4 h, and plateaued after 6 h (Figure 2A and Table S3). Consistently, the addition of BSP stopped CyPF$_6$ uptake for the first 8 h, with an 84 $\pm$ 12% decrease in CyPF$_6$ uptake after 24 h. Moreover, DMOG addition increased the rate of CyPF$_6$ uptake. Compared to CyPF$_6$, CyFPhB displayed a delayed cellular uptake with a steady increase over 24 h (Figure 2B and Table S3). Addition of BSP decreased the cellular uptake of CyFPhB by 80 $\pm$ 14% of uptake at 24 h. Furthermore, DMOG treatment increased the initial rate of uptake and plateaued at 12 h. Cellular uptake of CyTPFB was significantly retarded compared to that of CyPF$_6$, reaching a maximal uptake at 24 h. Addition of BSP decreased the cellular uptake of CyTPFB by 71 $\pm$ 6% (Figure 2C and Table S3). These results indicate that Oatps mediate the cellular uptake of CyPF$_6$, CyFPhB, and CyTPFB in 6DT1 cells.

Solution Absorption
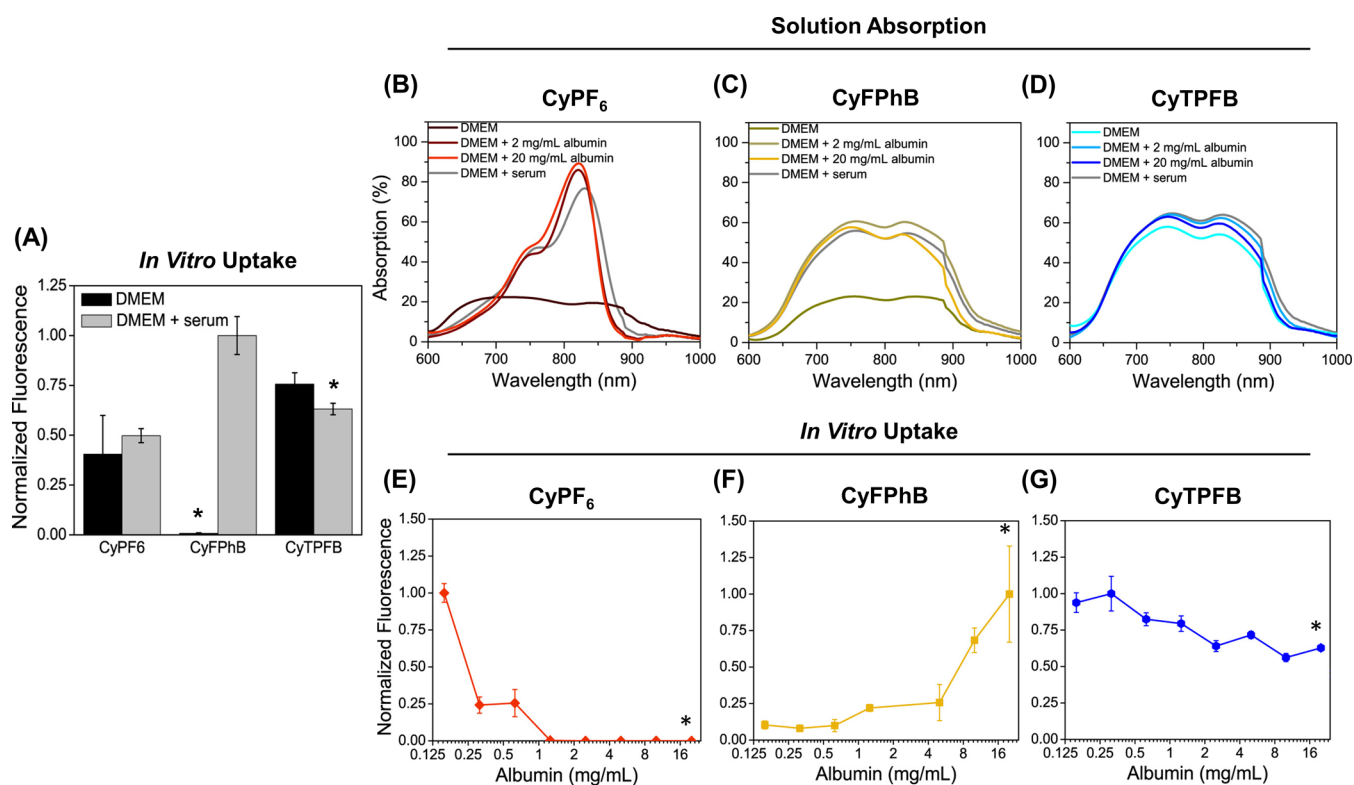

In Vitro Uptake

Figure 3. Albumin plays a critical role in organic salt stability and uptake. (A) 6DT1 cells were incubated in serum-free media (DMEM) and complete media (DMEM + serum) for 24 h with indicated organic salts. UV−Vis spectroscopy was used to characterize 5 μM (B) CyPF$_6$, (C) CyFPhB, and (D) CyTPFB in DMEM with increasing amounts of bovine serum albumin. Complete spectra can be found in Figure S3. 6DT1 cells were incubated with albumin in DMEM with (E) 1 μM CyPF$_6$, (F) 5 μM CyFPhB, and (G) 15 μM CyTPFB. Data are displayed as means ± S.D., $n = 3$. Statistically significant differences (p-value <0.05) between initial albumin concentration and final albumin concentration are marked with asterisks.

Noting the differences in cellular uptake kinetic trends for CyPF$_6$, CyFPhB, and CyTPFB and previously reported ζ-potentials, which could cause differences in protein affinity,[35] we examined additional endocytotic mechanisms of cellular uptake. No difference in organic salt uptake was observed upon incubation with various endocytotic inhibitors including dynasore, methyl-β-cyclodextrin, and amiloride (Figure S4). Interestingly, notable differences in uptake were observed in serum-free culture medium: CyFPhB uptake decreased dramatically when cells were incubated in culture medium without serum, while CyPF$_6$ and CyTPFB showed similar levels of uptake (Figure 3A). To determine if this increase in cellular uptake was mediated by changes to organic salt structure in the presence of serum, UV−Vis spectroscopy was performed on organic salts in DMEM, DMEM + serum, and DMEM with increasing concentrations of bovine serum albumin, the most abundant protein in serum.[48] The results showed that albumin and serum destabilized CyPF$_6$ nanoparticles to form monomers, as can be seen by spectral narrowing of the peaks (Figure 3B). In contrast, albumin increased CyFPhB nanoparticle solubility based on the increase in overall absorption (Figure 3C); however, albumin did not impact nanoparticle stability (Figure S5). CyTPFB maintained a stable nanoparticle solubility in all solutions with only a minimal increase in the solubility with increasing albumin (Figure 3D). These trends were also observed in complete cell media, indicating that albumin interaction has a significant impact on biological systems.

To further determine the effect of albumin on the cellular uptake of organic salts, 6DT1 cells were incubated in serial dilutions of purified bovine serum albumin in culture medium with each organic salt. Albumin stabilized the CyPF$_6$ cyanine monomer in an aqueous solution; however, increasing levels of BSA inhibit in vitro uptake (Figure 3E). In contrast, albumin was required for CyFPhB uptake; the intracellular fluorescence signals were increased with increasing albumin concentrations in a dose-dependent manner (Figure 3F). CyTPFB cellular uptake was independent of albumin concentrations, as uptake declined with the addition of albumin (Figure 3G). Cell viability was not affected by DMOG, BSP, or BSA in the presence or absence of organic salts (Figure S6), suggesting that reduced fluorescence following BSP treatment was not due to cell death. We further verified that albumin had no significant effects in decreasing the fluorescent quantum yields of organic salts (Figure S7). These results imply that Oatps mediate the cellular uptake of CyPF$_6$, CyFPhB, and CyTPFB. Moreover, albumin further mediates the uptake of CyFPhB.

Organic Salts Display Differential In Vivo Biodistribution. To verify trends observed in vitro and demonstrate potential clinical applications, we further performed in vivo experiments. FVB mice received an orthotopic injection of 10,000 syngeneic 6DT1 mammary cancer cells into the right fourth mammary fat pad. At 9 days post injection, a palpable tumor was formed, and mice received an intravenous injection of CyPF$_6$, CyFPhB, or CyTPFB through the tail vein. Biodistribution of organic salts was tracked using a fluorescent stereomicroscope, which allowed the monitoring of tumor
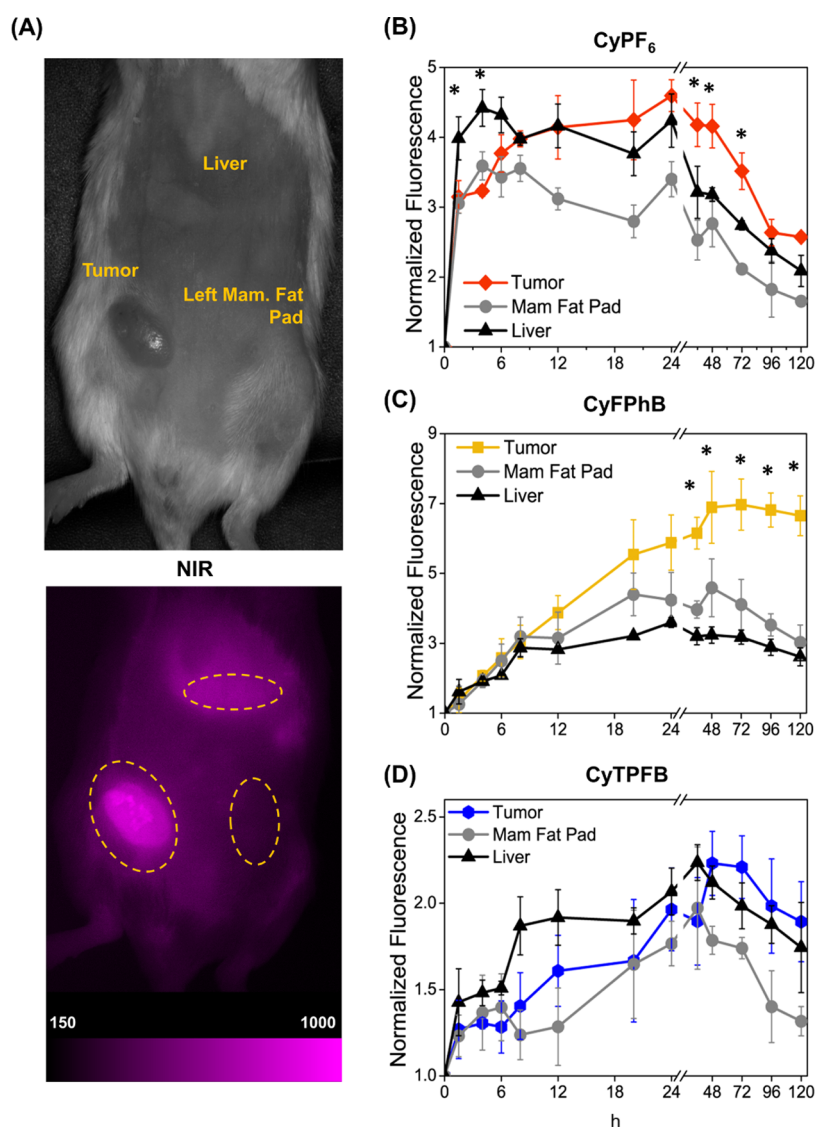
Figure 4. *In vivo* biodistribution data show that organic salts preferentially accumulate and are retained within 6DT1 mammary tumors. Following 6DT1 mammary tumor formation, mice received a tail vein injection of 1 μmol/kg CyPF$_6$, 3 μmol/kg CyFPhB, or 5 μmol/kg CyTPFB. (A) NIR fluorescence from the tumor-bearing fourth right mammary fat pad (tumor), liver (liver), and left fourth mammary fat pad (left mam. fat pad) was measured to determine the biodistribution of organic salts. The picture is a mouse dosed with 1 μmol/kg CyPF$_6$ at 48 h. Fluorescence intensity was normalized to a vehicle control. Normalized fluorescence of (B) CyPF$_6$, (C) CyFPhB, and (D) CyTPFB was measured in the tumor-bearing fourth right mammary fat pad (tumor), liver (liver), and left fourth mammary fat pad (mam fat pad). Data are displayed as means $\pm$ S.D., n = 3. Statistically significant differences (*p*-value <0.05) between tissue fluorescent intensity are marked with asterisks.

localization and PS clearance from normal tissues. To assess *in vivo* biodistribution, fluorescence intensity was measured for 5 days from the tumor (located on the right mammary fat pad), the nontumor-bearing left mammary fat pad, and the liver (Figure 4A).

CyPF$_6$ was rapidly uptaken by all measured tissues within the first 12 h, with initial localization in the liver for 1.5−6 h, predominately. The maximal tumor uptake was at 24 h, with a modest tumor retention over 48 h before gradually diminishing after 72 h. The observed tumor clearance was slower than from normal tissues, with a difference in fluorescence at 48 h of 25 $\pm$ 5%; however, tumor fluorescence cleared rapidly with poor overall retention (Figure 4B). Tumor uptake of CyFPhB was found to be slower compared to that of CyPF$_6$ which reached a maximal uptake at 48 h (Figure 4C). The liver uptake of CyFPhB was negligible with similar levels of fluorescence signal to background tissue (*i.e.*, nontumor-bearing right left

mammary fat pad). Moreover, CyFPhB showed an exceptional tumor-specific uptake, reaching a 45 $\pm$ 10% increase in fluorescence signal from surrounding tissues over 48−72 h and stably retained for more than 120 h, demonstrating promising therapeutic potential for PDT. Furthermore, tumor and liver showed significantly reduced uptake of CyTPFB compared to both CyPF$_6$ and CyFPhB (Figure 4D). Collectively, these *in vivo* biodistribution results indicate that organic salts preferentially accumulate and are retained within 6DT1 tumors.

CyFPhB Is a Selectively Phototoxic Antitumor Agent When Combined with NIR Irradiation. To explore the potential effects of fluorescent organic salts as potent PSs for PDT, we further performed *in vivo* studies in FVB mice orthotopically injected with 6DT1 mammary cancer cells. Tumor-bearing mice were dosed with 1−5 μmol/kg of the indicated organic salt or vehicle control (Veh) and further
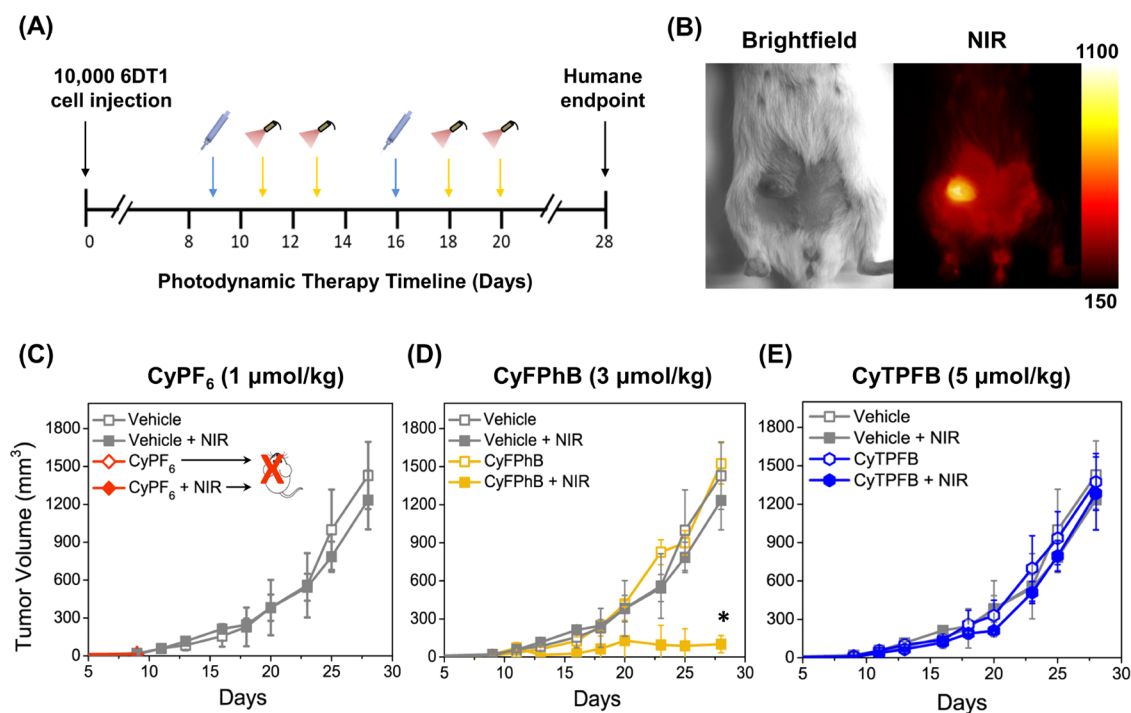
Figure 5. Counterion tuning of organic salts produces a potent photosensitizer (PS) for photodynamic therapy (PDT) in a mouse model of breast cancer. (A) Experimental overview of photodynamic therapy experimental timeline. FVB mice were injected with 10,000 6DT1 cells into the fourth right mammary fat pad. After 9 days, when a palpable tumor was present, mice were dosed with an organic salt *via* intravenous tail vein injection. After 2 days, the organic salt localized within the tumor and cleared from the surrounding offsite tissue. Mice were then irradiated with 150 J/cm^2 of 850 nm near-infrared light (NIR) at 48 and 96 h following organic salt administration. This PDT regimen was repeated 1 week after the first organic salt injection. Tumor growth was monitored throughout the course of the experiment with manual caliper measurement for 28 days when mice are euthanized due to tumor burden. (B) Representative image of tumor-specific localization of organic salts prior to NIR light irradiation. Pictured is an FVB mouse 44 h post IV injection of 5 μmol/kg CyFPhB. Tumor volume was measured in tumor-bearing mice treated with vehicle (Veh) or (C) 5 μmol/kg CyPF$_6$, (D) 3 μmol/kg CyFPhB, or (E) 5 μmol/kg CyTPFB with (+NIR) or without NIR irradiation. Data are displayed as means ± S.D., n = 4. Error bars represent S.D. Statistically significant differences (p-value <0.05) in CyFPhB + NIR tumor volumes from control groups at endpoint are marked with asterisks (*).

irradiated with 150 J/cm^2 of 850 nm light (Veh + NIR, CyX + NIR) at 48 and 96 h following organic salt administration (Figure 5A,B). Tumor volume was monitored with caliper measurements, and mice were euthanized on day 28 due to tumor burden in control groups. Mouse health was monitored throughout the experiment by weight and visual inspection every other day as well as blood chemistry assays at endpoint.

Mice in the 5 μmol/kg CyPF$_6$ + NIR treatment group were all sacrificed within 24 h post injection (Figure 5C). Mice in the 3 μmol/kg CyPF$_6$ + NIR treatment group exhibited severe tail swelling, limiting treatment to only one course of the PDT protocol, and there were no observable changes to tumor growth or appearance following light irradiation (Figure S8). Mice treated with 1 μmol/kg CyPF$_6$ with or without NIR light irradiation did not display any discernible effect on tumor growth compared to control groups (Figure S9). A similar lack of effect was observed *in vivo* with CyI at low dosage (Figure S10), another highly cytotoxic combination previously reported *in vitro*.[32] A higher dosage (5 μmol/kg CyPF$_6$) of either cytotoxic compound led to mouse death.

CyFPhB + NIR treatment (3 μmol/kg) showed a potent antitumor effect in mice, with a 93% reduction in tumor volume compared to control groups at experimental endpoint (Figure 5D). Following the first light treatment on day 11, a bruise developed around the tumor, which then formed a black eschar. This is indicative of vascular-specific PDT, a combination of direct photodamage to the cancer cells and

ablation of the tumor vascular, which starves the tumor of nutrients.[50] Mice in the CyFPhB + NIR group, in which tumor growth was stopped, were all visually healthy at experimental endpoint. In contrast, mice in the remaining three control groups, which were treated with CyFPhB (without NIR irradiation), Veh (without NIR irradiation), and Veh + NIR, all displayed severe labored breathing and decreased activity by day 28 from unrestricted tumor growth.

Treatment with 5 μmol/kg CyTPFB with or without NIR light did not exhibit any antitumor effect in mice, and no differences in tumor volume were observed between any of the groups (Figure 5E). Additionally, all mice were visually healthy at experimental endpoint, suggesting that CyTPFB is nontoxic *in vivo* at approved maximum doses.

At experimental endpoint, mice were sacrificed, and tumors were collected, weighed, and analyzed histologically for further assessment of treatment response. The CyFPhB + NIR group displayed a 69% decrease in tumor weight compared to control groups, confirming volume calculations from caliper measurements (Figure 6A). A concern with many cancer treatments is that the treatment may drive selection to induce increased tumor malignancy, leading to recurrence and drug resistance.[51,52] To assess this, healthy margins of tumors were stained for Ki67, a proliferation biomarker commonly used to prognose tumor aggressiveness.[53,54] There was no increase in Ki67$^+$ nuclei in the CyFPhB + NIR group compared to that in the control groups, and all tumors were Ki67$^+$-low by percent-
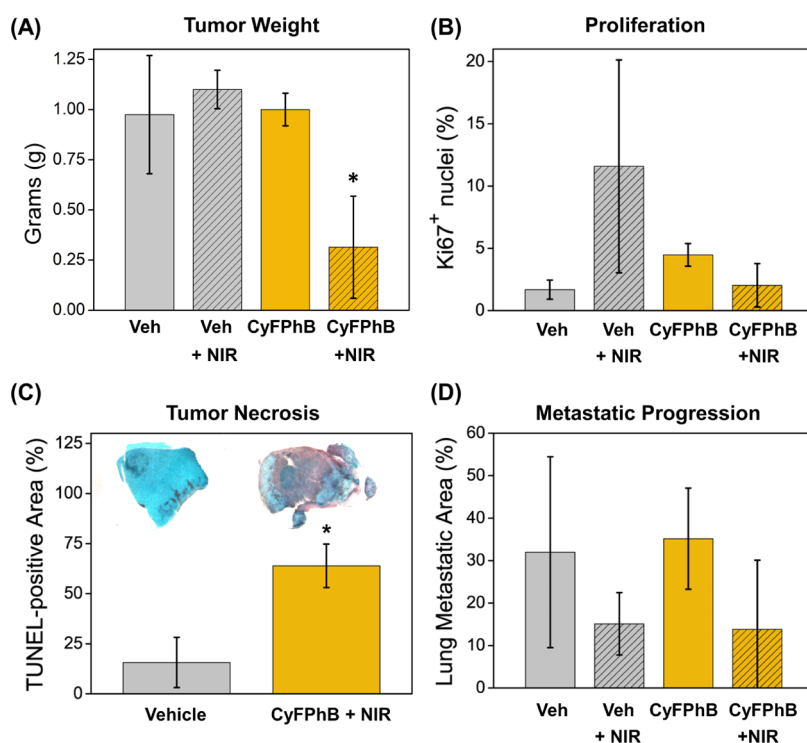
Figure 6. CyFPhB irradiated with NIR light induces an antitumor effect *via* tumor necrosis and impedes cancer progression in a breast cancer mouse model. At the end of the PDT experiment, tumor tissue was collected for further analysis of disease progression by (A) tumor weight, (B) Ki67 staining, (C) terminal deoxynucleotidyl transferase dUTP nick end labeling (TUNEL), and (D) lung histology, $n = 3$. Representative images of each group are shown in panel (C). Error bars represent SD. Statistically significant differences (p-value <0.05) in CyFPhB + NIR values from control groups are marked with asterisks (*).

positive nuclei (Figure 6B). Additionally, terminal deoxynucleotidyl transferase dUTP nick end labeling (TUNEL) assays were used to determine apoptotic and necrotic regions within the CyFPhB + NIR treated tumors.[55] TUNEL-stained cells were identified by brown staining within tumor cross sections. Samples taken at the experimental endpoint of 28 days no longer had any relevant necrotic regions (Figure S11). However, samples taken 72 h after PDT treatment displayed extensive TUNEL-staining, indicating tumor necrosis and apoptosis (Figures 6C and S12). This is likely due to a combination of PDT-induced photodamage directly to tumor and indirectly to the vasculature, which leads to tumor starvation and necrosis.[49] We have previously demonstrated that fluorescent organic salts preferentially accumulate in the mitochondria of cancer cells and generate mitochondrial superoxide.[35] Vasculature-PDT has been reported in clinically approved PS talaporfin sodium and is characterized by bruising at the irradiation site.[50]

To determine efficacy against metastatic disease, we further investigated the ability of CyFPhB + NIR to inhibit lung metastasis. Lungs were harvested, fixed in formalin, and sectioned for hematoxylin and eosin (H&E) staining. To quantify the extent of metastasis, we analyzed the percent metastatic area, which was identified by high-hematoxylin (blue) staining in nuclei-dense regions. While the average percentage of metastatic area was lower in the CyFPhB + NIR group, the difference was not statistically significant due to a wide degree of variation within groups (Figure 6D). Altogether, these results indicate that the combination of CyFPhB with NIR is an ideal PS for PDT *in vivo*, displaying a potent antitumor effect by triggering tumor apoptosis and necrosis in an orthotopic mouse model of breast cancer.

CyFPhB + NIR Antitumor Treatment Has Minimal Side Effects on Normal Tissues. To examine acute toxic side effects, we further monitored mouse weight and skin irritation at the site of light irradiation throughout the course of the experiment. Due to the aggressiveness of the 6DT1 breast cancer model, control tumors displayed minor ulceration prior to experimental endpoint. The CyFPhB + NIR group developed an eschar overlying the tumor following treatment but otherwise appeared to be in good overall condition at experimental endpoint with no significant decrease in mouse weight observed throughout the treatment course (Figure 7A). The minor difference in the final weight observed at the end of the experiment was not statistically significant and could be accounted for by the lack of a large tumor in CyFPhB + NIR mice. No mouse lost more than 10% of body weight throughout the course of the experiment.

Other clinical parameters were also examined to assess for evidence of end organ dysfunction affecting the kidneys and liver. Proteinuria was not detected in any group, as measured by urine reagent test strips. Liver injury was assessed at the end of the experiment by measuring serum levels of aspartate aminotransferase (AST) and alanine aminotransferase (ALT), biochemical markers of liver damage. All CyFPhB + NIR treatment mice displayed serum values within normal ranges and were unchanged compared to control treatment mice serum values (Figures 7B and S13).[51]

Additional potential offsite toxicity was assessed from tissue where residual fluorescence was noted upon *ex vivo* organ extraction, notably the spleen, kidneys, duodenum, and liver (Figure 7C). These tissues were fixed in formalin and underwent H&E staining. The CyFPhB + NIR group did not display any morphological alterations or increased
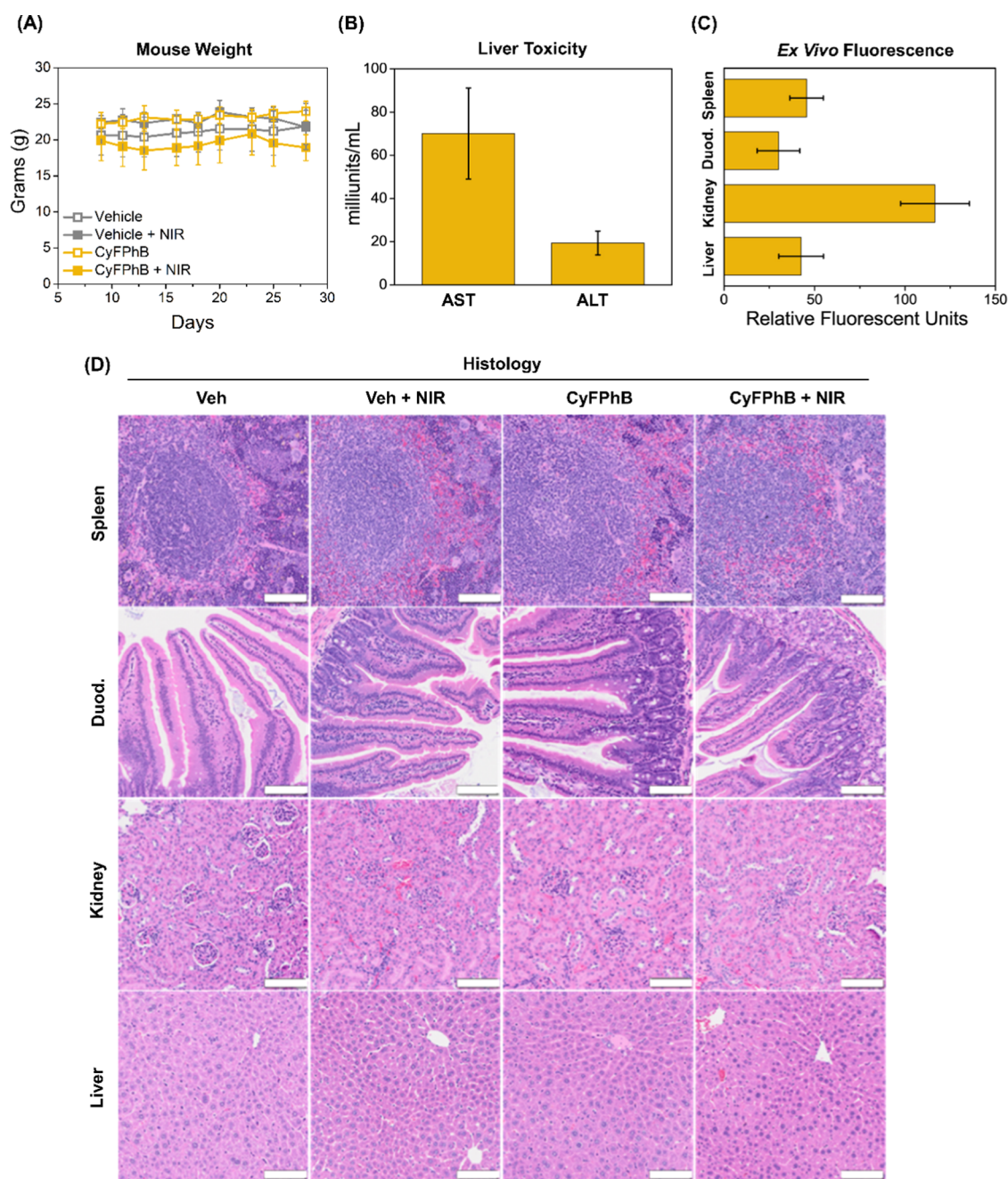
Figure 7. Minimal systemic toxicity observed with CyFPhB + NIR treatment in mice. (A) Mouse weight was monitored throughout the experiment. (B) Aspartate aminotransferase (AST) and alanine aminotransferase (ALT) serum levels were measured to assess liver damage at experimental endpoint in CyFPhB + NIR treatment mice. All measurements were within normal serum levels. (C) Residual fluorescence of normal biological tissues (spleen, duodenum, kidney, liver) was measured from CyFPhB + NIR treatment mice. (D) Representative histological images from each treatment group are shown. Scale bars: 100 μm. Data are displayed as means $\pm$ SD, $n = 4$.

inflammatory exudation (Figure 7D). Collectively, these data demonstrate that CyFPhB nanoparticles are a promising photosensitizing anticancer agent with minimal side effects.

CONCLUSIONS

Our findings demonstrate that our counterion tuning strategy has clinical potential and could transform PS engineering. We have demonstrated efficacious PDT in an immunocompetent mouse model of metastatic breast cancer, paving the way for translation to human cancer. Additional tumor-targeting may be achieved by the stable incorporation of these organic salt nanoparticles with antibody conjugation, which are common

engineering platforms for multiagent tumor delivery. Indeed, NIR-PSs are promising components for multimodal synergistic cancer therapy, as they have deep tissue imaging capabilities.[52−55] Reducing the nonspecific cytotoxicity and improving phototoxic yields of NIR organic salts with counterion tuning is a promising engineering strategy to advance tumor-specific PDT and cancer treatment.

EXPERIMENTAL SECTION

Synthesis and Purification of Organic Salts. Precursor salts (CyI and NaPF6, NaFPhB, or KTPFB) were dissolved in 5:1 methanol/dichloromethane (MeOH/DCM) mixtures and stirred at

room temperature under an inert nitrogen gas. The counterion precursor was added in 100% molar excess to drive the exchange of ions, and the product compounds precipitate out of solution after 5 min. The product was collected using vacuum filtration and rinsed with MeOH. The crude product was dissolved in minimal DCM and run through a silica gel plug with a DCM wash to remove unreacted precursors, side products, and other impurities. The product compound exiting the silica was identified by its color and elution time and collected. Excess DCM was removed in a rotary evaporator. The reaction yield and purity were confirmed by a high mass accuracy time-of-flight mass spectrometer coupled to an ultrahigh performance liquid chromatography (UPLC-MS) in positive mode to quantify cations and in negative mode to quantify anions. Typical reactions led to product yields of >60% with purities >95%. Reaction schemes and purification procedures described previously were used.[39,40]

Cell Culture Conditions. Mouse mammary carcinoma cells (6DT1) were cultured in Dulbecco's modified Eagle's medium (Cat. No. 10-017CM, Corning, NY) with 4.5 g/L glucose without sodium pyruvate with 10% heat-inactivated fetal bovine serum (Cat. No. F0392, Sigma-Aldrich, St. Louis, MO) supplemented with 2 mM glutamine and 1% penicillin and streptomycin (Cat. No. 15323671, Corning, NY). Cells were incubated in 37 °C with 5% CO_2 without light exposure. Fluorescent organic salts were dissolved in 5.6 mM dimethyl sulfoxide (Cat. No. D4540, Millipore Sigma-Aldrich, St. Louis, MO), and then further diluted in aqueous solution to form nanoparticles for various experiments.

Cell Viability Studies. 6DT1 cells were seeded at a density of 40,000 cells per well in 6-well tissue culture plates in dye-laced or vehicle (DMSO) media. After 24 h of incubation, media was aspirated and replaced with untreated media. Each well was irradiated with an 850 nm light-emitting diode (LED) lamp with an irradiation flux of 425 mW/cm^2 for 30 min in the incubator, and control cells were left in a dark incubator without irradiation. Following irradiation treatment, the media was replenished with fresh dye-laced media and allowed to incubate for another 24 h. The same procedure was done at 48 and 72 h, but the cells received no further dye-laced media after 72 h. The viable cell number was determined at 96 h using 4% trypan blue and a Nexcelom Cellometer Auto T4 cell counter. All assays were done with three biological replicates. The half-maximal inhibitory concentration (IC_{50}) was determined by plotting percent inhibition versus concentration and fitting using nonlinear regression with GraphPad Prism.

Kinetic Inhibition Studies. 6DT1 cells were seeded at a density of 25,000 cells per well in 24-well tissue culture plates. After 24 h, cells were preincubated for 15 min with 250 μM bromosulfophthalein (Cat. No. 21058, Cayman Chemical, Ann Arbor, MI), or 12 h with 1 mM dimethyloxalylglycine (Cat. No. D3695, Sigma-Aldrich, St. Louis, MO). Following the indicated preincubation with each inhibitor, the inhibitor-laced media was replaced with organic salts and inhibitor-laced media. For live cell imaging, the cells were washed three times with PBS and excited with 740 nm light. Fluorescence was measured using a Leica DMi8 microscope with a Cy7 filter cube, a PE4000 LED light source, a DFC9000GT camera, and LAS X imaging software. Cellular fluorescence was measured at the indicated time points, and all conditions were done in triplicate. Fluorescence was quantitated using ImageJ software. Curve fitting was performed with Origin Pro8 software by plotting relative fluorescent units versus time and using a dose−response sigmoidal equation.

Endocytosis Inhibition Studies. 6DT1 cells were seeded at a density of 25,000 cells per well in 24-well tissue culture plates. After reaching an 80−90% confluency, cells were serum-starved for 2 h. Following serum starvation, cells were preincubated either for 30 min in 3 mM amiloride (Cat. No. A7410, Sigma-Aldrich, St. Louis, MO), 1 h in 1 mM methyl-β-cyclodextrin (Cat. No. C4555, Sigma-Aldrich, St. Louis, MO), or for 20 min with 200 μM dynasore (Cat. No. 120192, Abcam). Following preincubation with various endocytotic inhibitors, inhibitor-laced media was replaced with organic salts and inhibitor-laced media. After 24 h, cellular fluorescence was measured as described above.

Ultraviolet−Visible (UV-Vis) Spectroscopy. Organic salts were diluted to a concentration of 5 μM in cell media and combined with the indicated concentrations of inhibitors. For albumin characterization, organic salts were diluted to a concentration of 5 μM in cell media, serum-free media (DMEM), and DMEM with the indicated concentrations of BSA. All dyes were characterized by a 25 UV−Vis spectrometer (Perkin-Elmer, Waltham, MA) in the wavelength range from 500 to 1100 nm in normal incidence transmission mode with a resolution of 1 nm and a 1.27 cm path length. Cell media with inhibitors was used as the solvent reference to remove reflections so that the absorption is calculated as 1-transmission.

Bovine Serum Albumin (BSA) Uptake Studies. Purified bovine serum albumin (Cat. No. A7030. Sigma-Aldrich, St. Louis, MO) was resuspended in serum-free media (DMEM) and was serially diluted to create the indicated concentrations. Concentrations of albumin used were determined based on the concentrations of fetal bovine serum used in cell media and in serum levels of mammals.[56] Indicated concentrations of fluorescent organic salts were added to solutions, and after 14 h, cellular fluorescence was measured as described above.

Photoluminescence. Photoluminescence (PL) spectra were collected using a Photon Technology International (PTI) spectrofluorometer for monomers of 5 μM $CyPF_6$ that was completely solubilized in DMSO or associated with 2 mg/mL BSA in DMEM without phenol red.

Orthotopic Cancer Model. All animal protocols were approved and performed in accordance with guidelines set by the Institute of Animal Care and Use Committee (IACUC) of Michigan State University (license number: 201900200). 6DT1 cells were harvested for tumor implantation at an 80% confluence while in the logarithmic phase of growth. 6DT1 cells (10,000) in 50 μL of sterile saline were inoculated into the right fourth mammary fat pad of 6−8 week old syngeneic FVB/NJ female mice (purchased from Jackson Laboratories, Bar Harbor, ME), as described previously.[41] Tumor growth was monitored every other day with external caliper measurements to determine tumor length and width to calculate volume, $V = L \times W^2/2$. Animal well-being was also monitored by recording mouse weight every other day and watching for potential skin irritation at the tumor site. The presence of protein in urine was monitored using urine reagent test strips (URS-1B/G/K/P, Cortez Diagnostics). Mice were euthanized at a 28 day endpoint, when the majority of control mice exhibit excessive morbidity due to tumor burden. Following euthanasia by carbon dioxide asphyxiation and subsequent cervical dislocation, tissues of interest were collected for further analysis.

***In Vivo* Imaging.** For biodistribution studies, at 11 days post orthotopic injection, tumor-bearing mice were dosed with 1 μmol/kg $CyPF_6$, 3 μmol/kg CyFPhB, or 5 μmol/kg CyTPFB *via* intravenous tail vein injection. For imaging, mice were anesthetized with 2.5% isoflurane and brightfield and NIR fluorescent images were taken at the indicated time points using a Leica M165FC stereoscope with a 740 nm PE4000 LED light source, a DFC9000GT camera, and LAS X imaging software. Using ImageJ, brightfield images were used to determine regions of interest (ROIs) for the tumor in the right fourth mammary fat pad, the liver, and the left fourth mammary fat pad. ROIs were then overlaid on the NIR fluorescent image for blinded quantitation of fluorescence intensity and normalized to a vehicle-injected mouse. The study ended after 5 days upon tumor ulceration due to rapid tumor growth.

Photodynamic Therapy. At 9 days post orthotopic injection, tumor-bearing mice were randomly divided into four treatment groups: (1) vehicle injection (Veh), (2) organic salt injection (CyX), (3) vehicle injection with NIR light irradiation (Veh + NIR), and (4) organic salt injection with NIR light irradiation (CyX + NIR). Organic salts were injected on day 9 after a palpable tumor was formed. For organic salt injection treatment groups (2 and 4), mice were given a 1−5 μmol/kg intravenous injection of a fluorescent organic salt dissolved in 5% DMSO and 0.03% Tween 20 in 100 μL of sterile saline prior to injection through the lateral tail vein. Vehicle groups (1 and 3) received a tail vein injection of 5% DMSO and 0.03% Tween 20 in 100 μL of sterile saline. ImageJ software was used to quantitate the relative brightness and localization within tumor

tissues relative to normal tissues at various time points throughout the experimental study. At 48 h post IV injection of the organic salt, NIR light irradiation groups (3 and 4) were anesthetized with 2.5% isoflurane, placed on a heated pad, and underwent tumor irradiation with an 850 nm LED. Mice received a 120−150 J/cm^2 dose over 15−20 min, depending on previously decided treatment conditions. This was repeated 48 h later. A week following the first organic salt IV injection, the PDT treatment was repeated.

Histology. All histologic preparation and immunohistochemistry staining were performed by the Investigative HistoPathology Laboratory at Michigan State University. Tumor, lung, spleen, kidney, liver, and duodenum were harvested, fixed in formalin, embedded in paraffin, sectioned, and stained with hematoxylin and eosin (H&E) for qualitative analysis. Tissues were visualized using an Olympus VS200 research slide scanner at a 20× magnification.

Ki67 Nuclei Staining Assessment. Ki67 staining was measured using images taken from healthy cross sections of tumors. Image processing was performed in ImageJ. The color images were first deconvoluted into hematoxylin (H) and diaminobenzidine (DAB) color channels using Color Deconvolution ("H DAB" deconvolution matrix). Deconvoluted H and DAB images were saved as new TIFF images. For each image, smoothing was applied 5 times, then Auto Local Threshold was performed using Phansalkar's's algorithm to detect stained nuclei. Stained nuclei were counted using Analyze Particles (minimum size 30, minimum circularity 0.3). To check that threshold parameters were appropriate, several output images were manually inspected to confirm that visually identifiable nuclei were properly counted. The percent Ki67$^+$ nuclei were calculated as the ratio of DAB-stained nuclei counts (representing proliferating cells) to H-stained nuclei counts (representing all cells) for each tumor.

TUNEL-Area Quantification. Terminal deoxynucleotidyl transferase-mediated dUTP nick end labeling (TUNEL) assays were evaluated using ImageJ to determine the percentage of necrotic to the total area of each tumor cross section. Images were acquired using a Leica M165FC stereomicroscope operated at a 1.6× magnification. Images were duplicated, smoothed to reduce artifacts, and color thresholding was used to select either the TUNEL$^+$ area or the entire tumor area. Representative thresholding can be found in Figures S8 and S9.

Metastatic Lung Area Assessment. Microscope images of lung histology slides were analyzed using ImageJ. Colors were converted using "Dichromacy > Tritanope" filter and then split into three channels, and the "blue" channel showing high overall intensity was subtracted from the "red" channel showing high selective intensity in high-hematoxylin tumor tissue regions. The resulting images show that the selective highlighting of tumor tissue region was then smoothed to reduce thresholding artifacts and finally thresholding was applied using auto local threshold with Phansalkar's's algorithm to quantitate the area of tumor tissue regions. Image processing workflows described previously were used.[42]

Alanine Aminotransferase (ALT) and Aspartate Aminotransferase (AST) Assays. Serum levels for alanine aminotransferase (Cat. No. MAK052, Sigma-Aldrich, St. Louis, MO) and aspartate aminotransferase (Cat. No. MAK055, Sigma-Aldrich, St. Louis, MO) were measured using commercially available kits according to the manufacturer's protocol. Samples were run in duplicate and averaged for analysis, before averaging levels for each treatment group.

Statistical Analyses. Statistical analyses were performed using an unpaired Student's *t*-test, and all error bars are representative of standard deviation, except where otherwise noted. All displayed data have a minimum of three biological replicates. Curve fittings were done using Origin Pro8 and GraphPad Prism software. *P*-values <0.05 are reported as statistically significant (*).

■ ASSOCIATED CONTENT

Ⓢ Supporting Information

The Supporting Information is available free of charge at https://pubs.acs.org/doi/10.1021/acsami.2c16252.

Additional characterization of organic salts, ROS measurements, viability studies, tumor growth studies, representative TUNEL assay color thresholds; serum levels of liver enzymes, half-maximal inhibitory concentrations, gene expression values, and sigmoidal curve fitting values (PDF)

■ AUTHOR INFORMATION

Corresponding Authors

Richard R. Lunt − *Department of Chemical Engineering and Materials Science and Department of Physics and Astronomy, Michigan State University, East Lansing, Michigan 48824, United States;* ⓞ orcid.org/0000-0003-4248-6312; Email: rlunt@msu.edu

Sophia Y. Lunt − *Department of Biochemistry and Molecular Biology, Michigan State University, East Lansing, Michigan 48824, United States; Department of Chemical Engineering and Materials Science, Michigan State University, East Lansing, Michigan 48824, United States;* ⓞ orcid.org/0000-0003-4522-6065; Email: sophia@msu.edu

Authors

Deanna Broadwater − *Department of Biochemistry and Molecular Biology, Michigan State University, East Lansing, Michigan 48824, United States*

Hyllana C. D. Medeiros − *Department of Biochemistry and Molecular Biology, Michigan State University, East Lansing, Michigan 48824, United States*

Matthew Bates − *Department of Chemical Engineering and Materials Science, Michigan State University, East Lansing, Michigan 48824, United States*

Amir Roshanzadeh − *Department of Biochemistry and Molecular Biology, Michigan State University, East Lansing, Michigan 48824, United States*

Shao Thing Teoh − *Department of Biochemistry and Molecular Biology, Michigan State University, East Lansing, Michigan 48824, United States*

Martin P. Ogrodzinski − *Department of Biochemistry and Molecular Biology, Michigan State University, East Lansing, Michigan 48824, United States; Department of Physiology, Michigan State University, East Lansing, Michigan 48824, United States*

Babak Borhan − *Department of Chemistry, Michigan State University, East Lansing, Michigan 48824, United States;* ⓞ orcid.org/0000-0002-3193-0732

Complete contact information is available at: https://pubs.acs.org/10.1021/acsami.2c16252

Author Contributions

D.B.: investigation, methodology, formal analysis, and writing—original draft. H.C.D.M.: investigation, formal analysis, visualization, and validation. M.B.: methodology, formal analysis, and visualization. A.R.: investigation, validation, and writing—review and editing. S.T.T. and M.P.O.: methodology and visualization. B.B.: resources. R.R.L.: conceptualization, methodology, writing—review and editing, supervision, project administration, and funding acquisition. S.Y.L.: conceptualization, methodology, writing—review and editing, supervision, project administration, and funding acquisition.

Notes

The authors declare no competing financial interest.

■ REFERENCES

(1) Lee, C. H.; Kim, K. W.; Lee, S. M.; Kim, S. Y. Dose-Dependent Effects of Resveratrol on Cisplatin-Induced Hearing Loss. *Int. J. Mol. Sci.* **2021**, *22*, No. 113.

(2) Broadwater, D.; Medeiros, H. C. D.; Lunt, R. R.; Lunt, S. Y. Current Advances in Photoactive Agents for Cancer Imaging and Therapy. *Annu. Rev. Biomed. Eng.* **2021**, *23*, 29−60.

(3) Dougherty, T. J.; Gomer, C. J.; Henderson, B. W.; Jori, G.; Kessel, D.; Korbelik, M.; Moan, J.; Peng, Q. Photodynamic Therapy. *J. Natl. Cancer Inst.* **1998**, *90*, 889−905.

(4) Wang, R.; Li, X.; Yoon, J. Organelle-Targeted Photosensitizers for Precision Photodynamic Therapy. *ACS Appl. Mater. Interfaces* **2021**, *13*, 19543−19571.

(5) Chance, B. Near-Infrared Images Using Continuous, Phase-Modulated, and Pulsed Light with Quantitation of Blood and Blood Oxygenationa. *Ann. N. Y. Acad. Sci.* **1998**, *838*, 29−45.

(6) Wäldchen, S.; Lehmann, J.; Klein, T.; van de Linde, S.; Sauer, M. Light-Induced Cell Damage in Live-Cell Super-Resolution Microscopy. *Sci. Rep.* **2015**, *5*, No. 15348.

(7) Yu, X.; Han, N.; Dong, Z.; Dang, Y.; Zhang, Q.; Hu, W.; Wang, C.; Du, S.; Lu, Y. Combined Chemo−Immuno−Photothermal Therapy for Effective Cancer Treatment via an All-in-One and One-for-All Nanoplatform. *ACS Appl. Mater. Interfaces* **2022**, *14*, 42988−43009.

(8) Zhang, G.; Li, K.; He, S.; Wang, L.; Guan, S.; Zhou, S.; Xu, B. Electron Donor−Acceptor Effect-Induced Organic/Inorganic Nanohybrids with Low Energy Gap for Highly Efficient Photothermal Therapy. *ACS Appl. Mater. Interfaces* **2021**, *13*, 17920−17930.

(9) Ma, X.; Huang, Y.; Abedi, S. A. A.; Kim, H.; Davin, T. T. B.; Liu, X.; Yang, W.-C.; Sun, Y.; Liu, S. H.; Yin, J.; Yoon, J.; Yang, G.-F. Rational Design and Application of an Indolium-Derived Heptamethine Cyanine with Record-Long Second Near-Infrared Emission. *CCS Chem.* **2022**, *4*, 1961−1976.

(10) Usama, S. M.; Thavornpradit, S.; Burgess, K. Optimized Heptamethine Cyanines for Photodynamic Therapy. *ACS Appl. Bio Mater.* **2018**, *1*, 1195−1205.

(11) Wu, J.; Pan, D.; Chung, L. W. K. Near-Infrared Fluorescence and Nuclear Imaging and Targeting of Prostate Cancer. *Transl. Androl. Urol.* **2013**, *2*, 254−264.

(12) Bhattarai, P.; Dai, Z. Cyanine Based Nanoprobes for Cancer Theranostics. *Adv. Healthcare Mater.* **2017**, *6*, No. 1700262.

(13) Zhang, Y.; Zhao, M.; Fang, J.; Ye, S.; Wang, A.; Zhao, Y.; Cui, C.; He, L.; Shi, H. Smart On-Site Immobilizable Near-Infrared II Fluorescent Nanoprobes for Ultra-Long-Term Imaging-Guided Tumor Surgery and Photothermal Therapy. *ACS Appl. Mater. Interfaces* **2021**, *13*, 12857−12865.

(14) Jewell, E. L.; Huang, J. J.; Abu-Rustum, N. R.; Gardner, G. J.; Brown, C. L.; Sonoda, Y.; Barakat, R. R.; Levine, D. A.; Leitao, M. M. Detection of Sentinel Lymph Nodes in Minimally Invasive Surgery Using Indocyanine Green and Near-Infrared Fluorescence Imaging for Uterine and Cervical Malignancies. *Gynecol. Oncol.* **2014**, *133*, 274−277.

(15) Hope-Ross, M.; Yannuzzi, L. A.; Gragoudas, E. S.; Guyer, D. R.; Slakter, J. S.; Sorenson, J. A.; Krupsky, S.; Orlock, D. A.; Puliafito, C. A. Adverse Reactions Due to Indocyanine Green. *Ophthalmology* **1994**, *101*, 529−533.

(16) Wang, H.; Li, X.; Tse, B. W.-C.; Yang, H.; Thorling, C. A.; Liu, Y.; Touraud, M.; Chouane, J. B.; Liu, X.; Roberts, M. S.; Liang, X. Indocyanine Green-Incorporating Nanoparticles for Cancer Theranostics. *Theranostics* **2018**, *8*, 1227−1242.

(17) Choi, C. H. J.; Alabi, C. A.; Webster, P.; Davis, M. E. Mechanism of Active Targeting in Solid Tumors with Transferrin-Containing Gold Nanoparticles. *Proc. Natl. Acad. Sci. U.S.A.* **2010**, *107*, 1235−1240.

(18) Bolleddula, J.; Shah, A.; Shadid, M.; Kamali, A.; Smith, M. D.; Chowdhury, S. K. Pharmacokinetics and Catabolism of [3H]TAK-164, a Guanylyl Cyclase C Targeted Antibody-Drug Conjugate. *Drug Metab. Dispos.* **2020**, *48*, 1239−1245.

(19) Shah, D. K.; Haddish-Berhane, N.; Betts, A. Bench to Bedside Translation of Antibody Drug Conjugates Using a Multiscale Mechanistic PK/PD Model: A Case Study with Brentuximab-Vedotin. *J. Pharmacokinet. Pharmacodyn.* **2012**, *39*, 643−659.

(20) Dougherty, T. J.; Cooper, M. T.; Mang, T. S. Cutaneous Phototoxic Occurrences in Patients Receiving Photofrin. *Lasers Surg. Med.* **1990**, *10*, 485−488.

(21) Yom, S. S.; Busch, T. M.; Friedberg, J. S.; Wileyto, E. P.; Smith, D.; Glatstein, E.; Hahn, S. M. Elevated Serum Cytokine Levels in Mesothelioma Patients Who Have Undergone Pleurectomy or Extrapleural Pneumonectomy and Adjuvant Intraoperative Photodynamic Therapy. *Photochem. Photobiol.* **2003**, *78*, 75−81.

(22) Cooper, E.; Choi, P. J.; Denny, W. A.; Jose, J.; Dragunow, M.; Park, T. I.-H. The Use of Heptamethine Cyanine Dyes as Drug-Conjugate Systems in the Treatment of Primary and Metastatic Brain Tumors. *Front. Oncol.* **2021**, *11*, No. 1336.

(23) Shi, C.; Wu, J. B.; Chu, G. C. Y.; Li, Q.; Wang, R.; Zhang, C.; Zhang, Y.; Kim, H. L.; Wang, J.; Zhau, H. E.; Pan, D.; Chung, L. W. K. Heptamethine Carbocyanine Dye-Mediated near-Infrared Imaging of Canine and Human Cancers through the HIF-1α/OATPs Signaling Axis. *Oncotarget* **2014**, *5*, 10114−10126.

(24) Hagenbuch, B.; Stieger, B. The SLCO (Former SLC21) Superfamily of Transporters. *Mol. Aspects Med.* **2013**, *34*, 396−412.

(25) Wu, J. B.; Shao, C.; Li, X.; Shi, C.; Li, Q.; Hu, P.; Chen, Y.-T.; Dou, X.; Sahu, D.; Li, W.; Harada, H.; Zhang, Y.; Wang, R.; Zhau, H. E.; Chung, L. W. K. Near-Infrared Fluorescence Imaging of Cancer Mediated by Tumor Hypoxia and HIF1α/OATPs Signaling Axis. *Biomaterials* **2014**, *35*, 8175−8185.

(26) Schulte, R. R.; Ho, R. H. Organic Anion Transporting Polypeptides: Emerging Roles in Cancer Pharmacology. *Mol. Pharmacol.* **2019**, *95*, 490−506.

(27) Yang, X.; Shi, C.; Tong, R.; Qian, W. P.; Zhau, H. E.; Wang, R.; Zhu, G.; Cheng, J.; Yang, V. W.; Cheng, T.; Henary, M.; Strekowski, L.; Chung, L. W. Near Infrared Heptamethine Cyanine Dye-Mediated Cancer Imaging. *Clin. Cancer Res.* **2010**, 2833−2844.

(28) Guan, Y.; Zhang, Y.; Zou, J.; Huang, L.-P.; Chordia, M. D.; Yue, W.; Wu, J.-J.; Pan, D.-F. Synthesis and Biological Evaluation of Genistein-IR783 Conjugate: Cancer Cell Targeted Delivery in MCF-7 for Superior Anti-Cancer Therapy. *Molecules* **2019**, *24*, No. E4120.

(29) Merlot, A. M.; Kalinowski, D. S.; Richardson, D. R. Unraveling the Mysteries of Serum Albumin—More than Just a Serum Protein. *Front. Physiol.* **2014**, *5*, No. 299.

(30) Davidson, S. M.; Jonas, O.; Keibler, M. A.; Hou, H. W.; Luengo, A.; Mayers, J. R.; Wyckoff, J.; Del Rosario, A. M.; Whitman, M.; Chin, C. R.; Condon, K. J.; Lammers, A.; Kellersberger, K. A.; Stall, B. K.; Stephanopoulos, G.; Bar-Sagi, D.; Han, J.; Rabinowitz, J. D.; Cima, M. J.; Langer, R.; Vander Heiden, M. G. Direct Evidence

for Cancer-Cell-Autonomous Extracellular Protein Catabolism in Pancreatic Tumors. *Nat. Med.* **2017**, *23*, 235−241.

(31) Usama, S. M.; Park, G. K.; Nomura, S.; Baek, Y.; Choi, H. S.; Burgess, K. Role of Albumin in Accumulation and Persistence of Tumor-Seeking Cyanine Dyes. *Bioconjugate Chem.* **2020**, *31*, 248−259.

(32) Matsumura, Y.; Maeda, H. A New Concept for Macromolecular Therapeutics in Cancer Chemotherapy: Mechanism of Tumoritropic Accumulation of Proteins and the Antitumor Agent Smancs. *Cancer Res.* **1986**, *46*, 6387−6392.

(33) Han, X.; Xu, X.; Tang, Y.; Zhu, F.; Tian, Y.; Liu, W.; He, D.; Lu, G.; Gu, Y.; Wang, S. BSA-Stabilized Mesoporous Organosilica Nanoparticles Reversed Chemotherapy Resistance of Anaplastic Thyroid Cancer by Increasing Drug Uptake and Reducing Cellular Efflux. *Front. Mol. Biosci.* **2020**, *7*, No. 610084.

(34) Miele, E.; Spinelli, G. P.; Miele, E.; Tomao, F.; Tomao, S. Albumin-Bound Formulation of Paclitaxel (Abraxane ABI-007) in the Treatment of Breast Cancer. *Int J Nanomedicine* **2009**, *4*, 99−105.

(35) Broadwater, D.; Bates, M.; Jayaram, M.; Young, M.; He, J.; Raithel, A. L.; Hamann, T. W.; Zhang, W.; Borhan, B.; Lunt, R. R.; Lunt, S. Y. Modulating Cellular Cytotoxicity and Phototoxicity of Fluorescent Organic Salts through Counterion Pairing. *Sci. Rep.* **2019**, *9*, No. 15288.

(36) Pei, X. F.; Noble, M. S.; Davoli, M. A.; Rosfjord, E.; Tilli, M. T.; Furth, P. A.; Russell, R.; Johnson, M. D.; Dickson, R. B. Explant-Cell Culture of Primary Mammary Tumors from MMTV-c-Myc Transgenic Mice. *In Vitro Cell. Dev. Biol.-Anim.* **2004**, *40*, 14−21.

(37) Ross, C.; Szczepanek, K.; Lee, M.; Yang, H.; Peer, C. J.; Kindrick, J.; Shankarappa, P.; Lin, Z.-W.; Sanford, J. D.; Figg, W. D.; Hunter, K. W. Metastasis-Specific Gene Expression in Autochthonous and Allograft Mouse Mammary Tumor Models: Stratification and Identification of Targetable Signatures. *Mol. Cancer Res.* **2020**, *18*, 1278−1289.

(38) Faraji, F.; Pang, Y.; Walker, R. C.; Nieves Borges, R.; Yang, L.; Hunter, K. W. Cadm1 Is a Metastasis Susceptibility Gene That Suppresses Metastasis by Modifying Tumor Interaction with the Cell-Mediated Immunity. *PLoS Genet.* **2012**, *8*, No. e1002926.

(39) Donohoe, C.; Senge, M. O.; Arnaut, L. G.; Gomes-da-Silva, L. C. Cell Death in Photodynamic Therapy: From Oxidative Stress to Anti-Tumor Immunity. *Biochim. Biophys. Acta, Rev. Cancer* **2019**, *1872*, No. 188308.

(40) Yang, Y.; Yang, H. H.; Hu, Y.; Watson, P. H.; Liu, H.; Geiger, T. R.; Anver, M. R.; Haines, D. C.; Martin, P.; Green, J. E.; Lee, M. P.; Hunter, K. W.; Wakefield, L. M. Immunocompetent Mouse Allograft Models for Development of Therapies to Target Breast Cancer Metastasis. *Oncotarget* **2017**, *8*, 30621−30643.

(41) Pari, A. A. A.; Singhal, M.; Augustin, H. G. Emerging Paradigms in Metastasis Research. *J. Exp. Med.* **2021**, *218*, No. e20190218.

(42) Chen, J.; Wang, Y.; Fang, Y.; Jiang, Z.; Wang, A.; Xue, J. Improved Photodynamic Anticancer Activity and Mechanisms of a Promising Zinc(II) Phthalocyanine-Quinoline Conjugate Photosensitizer in Vitro and in Vivo. *Biomed. Opt. Express* **2020**, *11*, 3900−3912.

(43) Csanaky, I. L.; Lu, H.; Zhang, Y.; Ogura, K.; Choudhuri, S.; Klaassen, C. D. Organic Anion−Transporting Polypeptide 1b2 (Oatp1b2) Is Important for the Hepatic Uptake of Unconjugated Bile Acids: Studies in Oatp1b2-Null Mice. *Hepatology* **2011**, *53*, 272−281.

(44) Desai, N.; Trieu, V.; Damascelli, B.; Soon-Shiong, P. SPARC Expression Correlates with Tumor Response to Albumin-Bound Paclitaxel in Head and Neck Cancer Patients. *Transl. Oncol.* **2009**, *2*, 59−64.

(45) Ghinea, N. Anti-Angiogenic Therapy: Albumin-Binding Proteins Could Mediate Mechanisms Underlying the Accumulation of Small Molecule Receptor Tyrosine Kinase Inhibitors in Normal Tissues with Potential Harmful Effects on Health. *Diseases* **2021**, *9*, No. 28.

(46) Zhao, N.; Zhang, C.; Zhao, Y.; Bai, B.; An, J.; Zhang, H.; Wu, J. B.; Shi, C. Optical Imaging of Gastric Cancer with Near-Infrared Heptamethine Carbocyanine Fluorescence Dyes. *Oncotarget* **2016**, *7*, 57277−57289.

(47) Zhang, S.; Ma, K.; Liu, Y.; Pan, X.; Chen, Q.; Qi, L.; Li, S. Stabilization of Hypoxia-Inducible Factor by DMOG Inhibits Development of Chronic Hypoxia−Induced Right Ventricular Remodeling. *J. Cardiovasc. Pharmacol.* **2016**, *67*, 68−75.

(48) Larsen, M. T.; Kuhlmann, M.; Hvam, M. L.; Howard, K. A. Albumin-Based Drug Delivery: Harnessing Nature to Cure Disease. *Mol. Cell. Ther.* **2016**, *4*, No. 3.

(49) Harrod-Kim, P. Tumor Ablation with Photodynamic Therapy: Introduction to Mechanism and Clinical Applications. *Journal of Vascular and Interventional Radiology* **2006**, *17*, 1441−1448.

(50) Suzuki, T.; Tanaka, M.; Sasaki, M.; Ichikawa, H.; Nishie, H.; Kataoka, H. Vascular Shutdown by Photodynamic Therapy Using Talaporfin Sodium. *Cancers* **2020**, *12*, No. 2369.

(51) Sher, Y.-P.; Hung, M.-C. Blood AST, ALT and UREA/BUN Level Analysis. *Bio-Protoc.* **2013**, *3*, No. e931.

(52) Chen, Q.; Feng, L.; Liu, J.; Zhu, W.; Dong, Z.; Wu, Y.; Liu, Z. Intelligent Albumin-MnO2 Nanoparticles as PH-/H2 O2 -Responsive Dissociable Nanocarriers to Modulate Tumor Hypoxia for Effective Combination Therapy. *Adv. Mater.* **2016**, *28*, 7129−7136.

(53) Zhang, Q.; Li, L. Photodynamic Combinational Therapy in Cancer Treatment. *J. BUON* **2018**, *23*, 561−567.

(54) Wei, X.; Zhang, C.; He, S.; Huang, J.; Huang, J.; Liew, S. S.; Zeng, Z.; Pu, K. A Dual-Locked Activatable Phototheranostic Probe for Biomarker-Regulated Photodynamic and Photothermal Cancer Therapy. *Angew. Chem., Int. Ed.* **2022**, *61*, No. e202202966.

(55) Zeng, Z.; Liew, S. S.; Wei, X.; Pu, K. Hemicyanine-Based Near-Infrared Activatable Probes for Imaging and Diagnosis of Diseases. *Angew. Chem., Int. Ed.* **2021**, *60*, 26454−26475.

(56) Francis, G. L. Albumin and Mammalian Cell Culture: Implications for Biotechnology Applications. *Cytotechnology* **2010**, *62*, 1−16.